International Journal of GEOMATE, June, 2022, Vol.22, Issue 94, pp.93-101
ISSN: 2186-2982 (P), 2186-2990 (O), Japan, DOI: https://doi.org/10.21660/2022.94.3290
Geotechnique, Construction Materials and Environment

TOPOGRAPHY INDUCED STRESS AND ITS INFLUENCE ON TUNNEL EXCAVATION IN HARD ROCKS – A NUMERICAL APPROACH

Wahid Ali[1,2], Hafeezur Rehman[2], *Rini Asnida Abdullah[1], Qiang Xie[3,4] and Yuxin Ban[3]

[1]School of Civil Engineering, Faculty of Engineering, Universiti Teknologi Malaysia, Malaysia
[2]Department of Mining Engineering, Baluchistan University of Information Technology, Engineering and Management Sciences (BUITEMS), Pakistan
[3]Key Laboratory of New Technology for Construction of Cities in Mountain Area, Ministry of Education, Chongqing University, China
[4]School of Civil Engineering, Chongqing University, China

*Corresponding Author, Received: 05 Feb. 2022, Revised: 18 Feb. 2022, Accepted: 10 March 2022

ABSTRACT: In-situ stress characterisation is essential for anticipating the viability of underground structures. In areas with rugged topography, the in-situ stress varies within short distances and cannot be characterized by limited in-situ stress measurements. The in-situ stress at a point below the ground surface results from the combined effect of topography, tectonic forces, material properties and many others. The impact of topography on subsurface in-situ stress can be significant in areas with rugged topography. In this study, 3D finite element modelling utilising the Digital Elevation Model of a tunnelling project site is used to characterise the in-situ stress. Gravity loading was assumed to simulate the impact of topography on the subsurface in-situ state of stress. The reliability of the results was validated by analysing the stress-induced brittle failures in a section of the tunnel. The simulated in-situ principal stresses and the corresponding stress-induced failure zones were in good agreement with the actual observations in the tunnel. The results suggest that the present-day topography dominates the in-situ stress in the study area.

Keywords: *In-situ stress; 3D numerical modelling; Topography; Stress-induced failure*

1. INTRODUCTION

In any underground project, the in-situ stress magnitudes and orientations are the most critical parameters that need attention during the site characterisation phase. During tunnelling or mining, at a greater depth, difficult ground conditions are encountered in highly stressed environments. In such cases, often, the stress level exceeds the loading capacity of laboratory testing, and it becomes difficult to characterise the rock behaviour under such highly confined stress conditions [1].

Underground caverns are often aligned parallel to the major principal stress [2]. In the case of misalignment, the deformation surrounding the underground excavation amplifies [3]. Stress-induced failures occur after excavation in the form of spalling in low confinement areas such as at the excavation boundary [4] and shear failure when the confinement exceeds 10% of the UCS (Unconfined Compressive Strength) of intact rock [1]. In extreme cases, the stress-induced instability appears in the form of a rockburst [5, 6].

Several authors developed empirical approaches to anticipate the in-situ spalling and crack initiation strength at the excavation boundary. According to Martin [4], failure initiates in massive to moderately jointed hard rock when the tangential stress at the excavation boundary reaches 0.3 to 0.5 times the UCS of intact rock. They also suggested that the in-situ crack initiation strength can be found by constant deviatoric stress (σ_{dev}) given by $\sigma_1 - \sigma_3 = 0.33$ UCS. Cai et al., 2004 [7] proposed a generalised crack initiation and crack damage threshold for rock masses. They defined the “crack initiation” as the onset of damage, and the “crack damage” as the onset of macroscopic fractures, i.e., the coalescence of cracks to form shear bands and tensile spalls. They found that the crack initiation and crack damage occur when the σ_{dev} magnitude becomes equal to 40 to 50%, 80 to 90% of UCS_{rm} (UCS of rock mass) for massive to moderately jointed rock masses respectively, and 50 to 60%, 90 to 100% of UCS_{rm} for moderately to highly jointed rock masses, respectively.

In-situ stress measurement techniques have been increasingly used for the last few decades. Ljunggren *et al.* [8] and Hudson *et al.* [9] summarised different in-situ stress measurement methods. Amadei and Stephansson [10] listed several factors and processes which contribute to the in-situ state of stress at a site, which include o Due to these contributing factors and the complex nature of rock masses, the in-situ stress cannot be determined accurately. Even in excellent quality rock conditions where rock is homogeneous, continuous, and linearly elastic, the in-situ stress magnitude and orientation can be determined with an error of ±10-20% [10]. Also, the rock masses are rarely homogenous and isotropic in a project site; thus, the in-situ stress measurement results may not represent the actual state of stress. Moreover, often a limited number of borehole base in-situ stress measurements are conducted to characterise the in-situ stress in a project site. The boreholes characterise the in-situ stress in a limited volume, and the lateral variation in the stress away from the borehole cannot be captured in this method [10].

The numerical modelling approach has gained significant attention from geotechnical engineers due to the recent advancement in software, hardware, and computing power. Finite element modelling (FEM) is commonly used to determine the stresses and strains in complex engineering problems, including soil or rock-structure interaction [11, 12]. The numerical modelling approach can be used to assess the influence of individual parameters that contribute to the in-situ state of stress. Such as the influence of gravity, topographic undulations, material heterogeneity, tectonic forces and unloading due to erosion. Several researchers have utilised numerical modelling approaches to investigate the near-surface stress tensors [13] and tectonics and topography effects on the in-situ stress state [14-16]. Others used numerical approaches to analyse the tunnel wall deformation using different tunnel shapes [17] and excavation sequences [18].

In this study, we simulated the 3D real topography to evaluate the influence of topographic undulations on the in-situ stress in a section of the Lowari Tunnel (Pakistan). Only gravity loading was considered, and the project site was assumed free from the influence of active tectonic stresses. The in-situ stress derived from the gravitational model was then implemented in a separate 3D model to simulate the excavation induced damage zones surrounding a section of the tunnel. The modelling results were compared with the stress-induced brittle failures observed in the respective tunnel section.

2. RESEARCH SIGNIFICANCE

The in-situ stress measurement is rarely conducted in underground engineering projects mainly because of higher costs. Three-dimensional numerical modelling presents an alternative method for in-situ stress characterisation. The in-situ stress represents the total stress at a point and is the outcome of the combined effect of many parameters. This study highlights the performance of the FEM based numerical approach for studying the proportion of individual parameters in the total stress. The study presents a detailed procedure, underlying assumptions and limitations of the FEM based numerical modelling for stress analysis. Moreover, this study guides geotechnical engineers and engineering geologists regarding model validation based on field observations and available empirical approaches.

3. FINITE ELEMENT IN-SITU STRESS MODELLING

3.1 Intact Rock and Rock Mass Properties

During the excavation stage of the Lowari Tunnel, the rock mass encountered along the tunnel consisted mainly of granite, granodiorite, and granite gneiss, of which granite was the most widespread. In this study, the project site's geology was simplified for the numerical models using a linear-elastic constitutive model with a generalised Hoek-Brown failure criterion. The uniaxial compressive strength (UCS) was determined from the intact rock specimens of granite in the laboratory. Strain gauges were attached to the core specimens during the UCS test to record the strain at a given amount of stress. The young's modulus and Poisson's ratio were determined based on an analysis of stress-strain data. The UCS values and the corresponding young's modulus derived from laboratory test data are shown in Fig.1a and b.

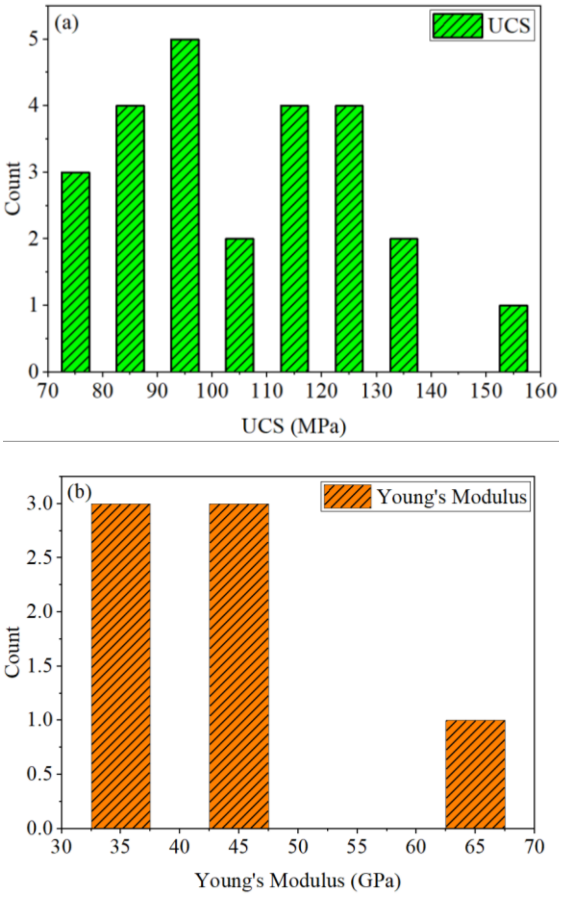

Fig.1 Magnitudes of Uniaxial compressive strength and young's modulus

The RQD (Rock Quality Designation) values were determined from the tunnel face mapping data using Palmstrom's [19] relationship between RQD and volumetric joint count (J_v). In the absence of GSI values based on direct observations of exposed rock surfaces, Hoek et al., 2013 [20] developed a relationship between GSI, joint condition rating ($JCond_{89}$) [21] and RQD and recommended its use for this purpose. Therefore, in this study, the following relation was used for estimating the GSI values;

$$GSI = 1.5JCond_{89} + RQD/2 \tag{1}$$

The distribution of RQD values derived from tunnel face mapping data and the corresponding GSI values are shown in Figs.2a and b. A mean value of the Geological Strength Index (GSI) was considered for the analysis.

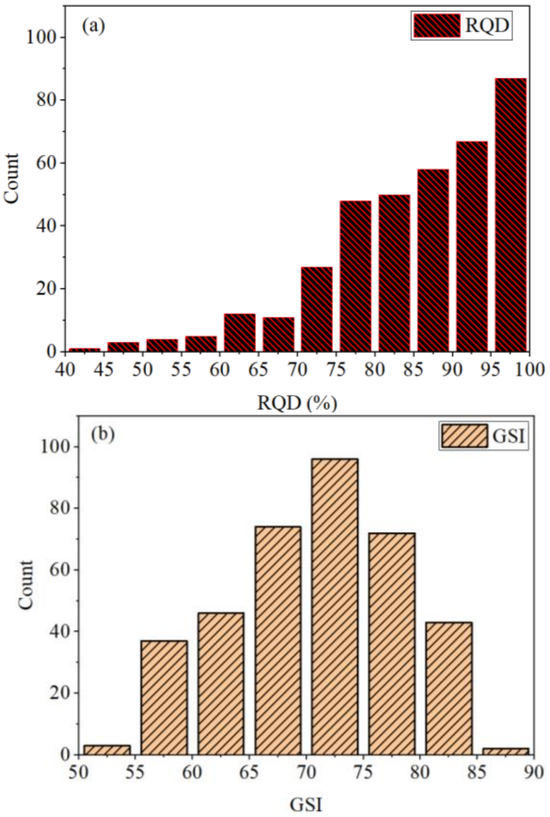

Fig.2 RQD and GSI values determined from tunnel face mapping data

Table 1 lists the mean values of the physical and mechanical properties of the rock. The data is used as input to the RSData version 5.009 [22] to determine the Hoek-Brown constants 'm_b', 's', and 'a' and the corresponding UCS and rock mass deformation modulus. The Hoek-Brown intact rock constant (m_i) for granite is considered here, and its value is taken from the suggested values in the RSData. A disturbance factor (D) of zero is assumed.

Table 1 Rock and rock mass parameters

Input to RSData	
Parameters	Values
Uniaxial Compressive Strength (σ_c) (MPa)	105
Geological Strength Index (GSI)	63
Hoek-Brown constant "m_i"	30
Young's Modulus (GPa)	45
Poisson' Ratio	0.25
Unit Weight (MN/m^3)	0.026
Disturbance factor	0
Output from RSData	
Parameters	Values
Hoek-Brown constant "m_b"	10.6
Hoek-Brown constant "s"	0.04
Hoek-Brown constant "a"	0.5
Uniaxial Compressive Strength of rock mass (UCS_{rm}) (MPa)	21
Rock mass deformation modulus (E_{rm}) (GPa)	33.8

3.2 Model Geometry Setup

In this study, the digital elevation model of the study area is used to establish an approximate realistic topography. The dimensions of the model are shown in Fig.3. We extended the vertical extent of the model 3 km below the tunnel elevation to reduce the boundary effect influencing the near-surface stresses. Also, the model's width is sufficiently extended to include the effective topography in the model.

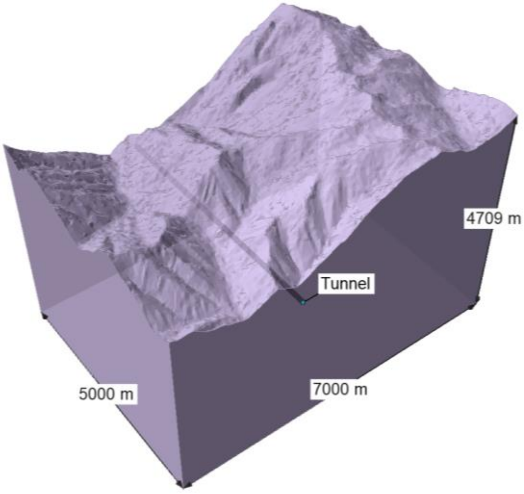

Fig.3 Digital elevation model of the study area

We discretised the model using 13.3 million four noded tetrahedra elements. A graded mesh and size ranging from 0.1 to 100 m were used. A cross-section of the model showing the mesh density distribution is shown in Fig.4. The mesh is denser surrounding the tunnel, which is suitable for the subsequent analysis.

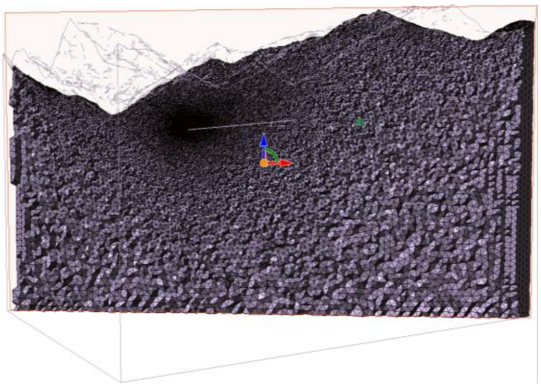

Fig.4 Mesh density across the model geometry

3.3 Material Model and Boundary Conditions

We used the RS3, a three-dimensional finite element program developed by Rocscience company, for stress analysis. A linear elastic model with isotropic rock mass properties is assumed. The generalised Hoek-Brown strength criterion was used to characterise the rock mass strength. The displacement along vertical and basal boundaries of the model was kept fixed; only boundary-parallel displacement was allowed. The boundary along the topography was kept as a free boundary.

3.3.1 Simulating the brittle failure in the tunnel

For validating the results of the gravitational model, we compared the simulated principal stresses with brittle failures reported during the excavation of the Lowari Tunnel. For this purpose, a section of the tunnel was selected where blasting damage with subsequent spalling was reported. The excavated cross-sections along a 100 m length of the selected tunnel section are shown in Fig.5. The cross-sections are superimposed to visualise a general shape of the excavated tunnel and to show an estimate of over-excavation beyond the design tunnel profile. Further details of the tunnel section are listed in Table 2.

Table 2 Details of the tunnel sections selected for the analysis

Chainage (m)	5114-5520
Section length (m)	406
Average overburden (m)	1157
Failure location	Crown and both sidewalls

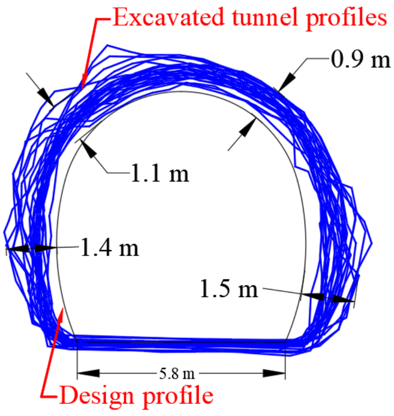

Fig.5 Sequential excavation of the selected tunnel section

To simulate the stress-induced failures in the selected tunnel section, an additional 3D numerical model was developed. The geometry was discretised using a graded mesh with 4-noded tetrahedra elements and an element size ranging from 0.1 to 5 m (see Fig. 6). Elastic material with Hoek-Brown brittle parameters, i.e., m_b = 0, s = 0.11, was selected based on the recommended method for simulating the stress-induced failures at low confinement or the excavation wall [23]. The principal stresses derived from the large-scale gravitational model were applied as constant loads in this model. A 36 m length of the tunnel section was excavated in twelve stages (Fig.7). The Strength Factor (SF), which represents the stress to strength ratio, was used to interpret the stress-induced failure zones in the tunnel. The SF value less than unity indicates overstressing or failure.

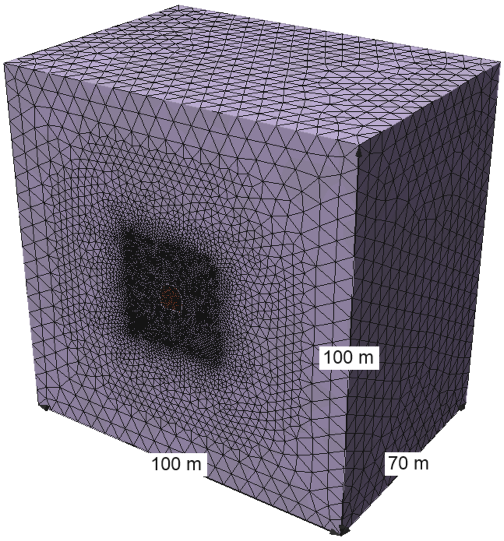

Fig.6 Model geometry and discretisation for simulating the tunnel excavation process

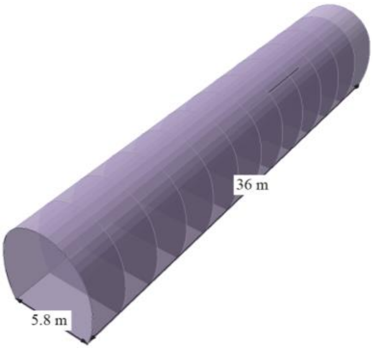

Fig.7 Sequential excavation of the selected tunnel section

3.3.2 Estimates of redistributed stresses due to tunnel excavation

The magnitude of the deviatoric stress (σ_{dev}) and the orientation of the principal stresses axes control the stress-induced damage near the excavation boundary [4, 24, 25]. It is, therefore, necessary to know the pre-excavation, during excavation and post-excavation σ_{dev} level along the alignment of the proposed underground excavation. As the tunnel excavation advances, dynamic changes in the magnitude and orientation of principal stresses occurs ahead of the tunnel face. These dynamic changes were monitored in the crown and walls of the tunnel. To investigate the onset of these dynamic changes, monitoring points were selected in the crown and wall of the tunnel (Fig.8). The location of the monitoring points was kept 18 m ahead of the tunnel face. Then the tunnel was sequentially excavated with a 3 m excavation round length. The change in the magnitude of deviatoric stress and the SF were monitored after each excavation round until the excavation face passed 18 m ahead of the location of the monitoring points, i.e., after a total 36 m excavation. The results from this model were then compared with the observed stress-induced failures in the respective tunnel section. The simulated stress-induced failures were also compared with different empirical and analytical approaches developed for assessing the brittle failure initiation and propagation.

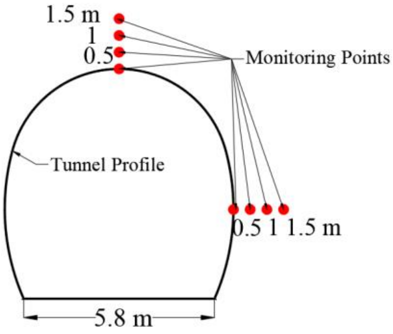

Fig.8 Position of monitoring points along the tunnel perimeter

4. RESULTS AND DISCUSSION

4.1 Interpretation of Results of Gravitational Model

In Fig.9, the spherical projections of the modelled principal stresses are presented. These plots are generated based on principal stress orientation data obtained from the gravitational model. The trends of principal stresses and maximum horizontal stress for the selected tunnel section are shown in Fig.9. The plunge of σ_1 ranges from 8-16°, which shows a horizontal to sub-horizontal σ_1 along the tunnel axis. The mean magnitudes of principal, horizontal and vertical stresses calculated by solving modelled 3D stress tensors are listed in Table 3. The maximum horizontal, minimum horizontal, and vertical stresses are denoted by σ_H, σ_h, and σ_v, respectively.

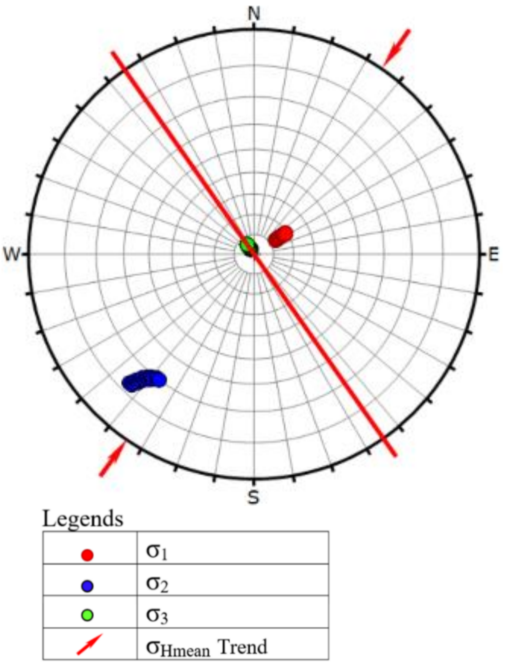

Fig.9 Lower hemisphere equal angle pole vector plots of modelled principal stresses.

Table 3 Mean stresses derived from gravitational model (all values are in MPa)

σ_1	σ_2	σ_3	σ_H	σ_h	σ_v
33.2	28.4	21	32.8	21	28.7

4.1.1. Comparison of model result with empirical approaches for stress-induced failures

In this section, the results from the numerical model developed for simulating the tunnel excavation process are compared with the different empirical approaches established for predicting the stress-induced failures in underground excavations. The change in σ_{dev} magnitude recorded at each of the monitoring points at the tunnel crown and wall are shown in Figs.10a and b. For comparison purposes, the brittle failure limits proposed by Martin [4] and Cai et al., 2004 [7] are also shown as horizontal lines in these figures. A sharp increase in the magnitude of σ_{dev} can be observed 3m ahead of the tunnel face, which continued to increase 3-6m behind the tunnel face and then gradually attains a maximum value of 15-18 m behind the tunnel face. As mentioned earlier, in the selected tunnel section, blast-induced damage followed by spalling was observed in the crown area. Here the σ_{dev} magnitude at the tunnel crown and wall exceeded both the Martin [4] and Cai et al., 2004 [7] suggested limits. Thus, the results suggest stress-induced failures both in the crown and wall area of the tunnel.

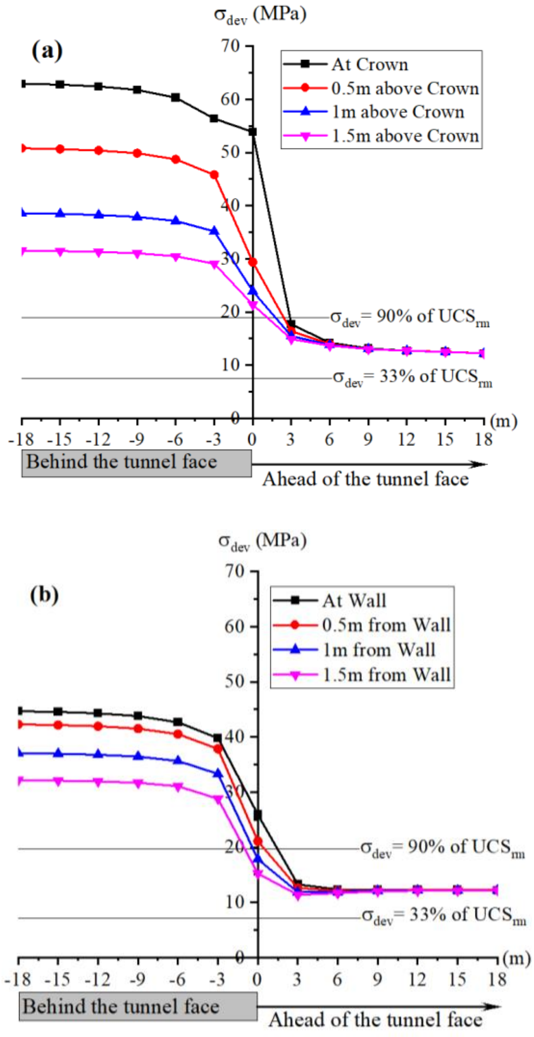

Fig.10 Comparison of σ_{dev} magnitude at the monitoring points for a given position of the tunnel face, a) At the crown, and b) at the tunnel wall.

Similarly, Figs.11a and b represent the monitored SF (Strength Factor) values in the selected tunnel section. A minimum SF = 0.58 and SF = 0.81 were recorded at the crown and wall, respectively. These results also indicate stress-induced failures in the tunnel crown and wall. The SF<1 is up to approximately 1 m above the crown, thereby indicating deep stress-induced failure in the crown.

In Fig.12, the SF contours surrounding the tunnel at a location 15m behind the tunnel face are shown. The location and depth of failed rock along the tunnel perimeter can be observed in this figure.

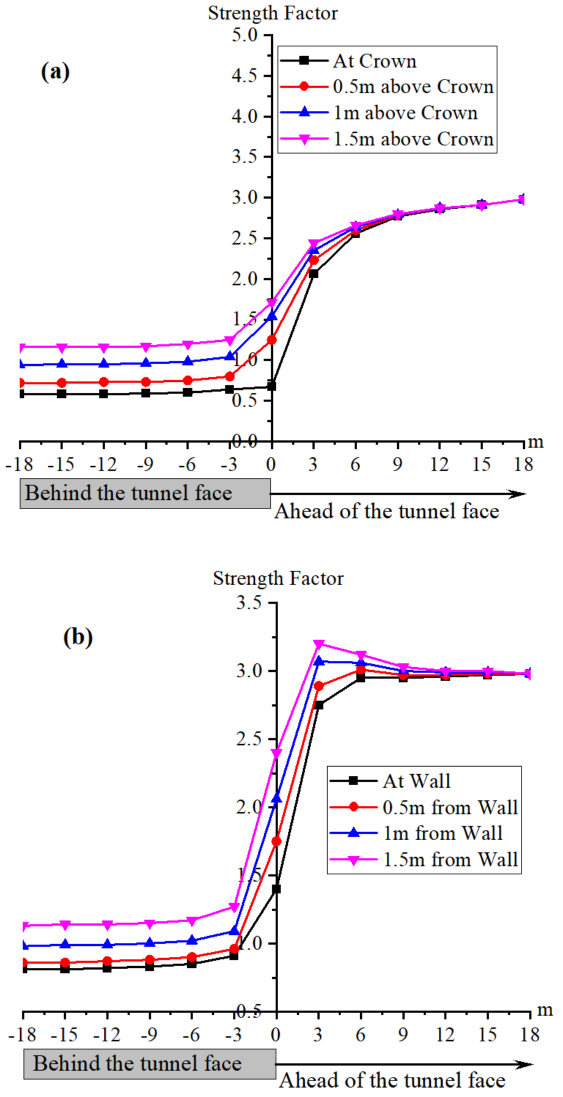

Fig.11 Comparison of Strength Factors at the monitoring points for a given position of the tunnel face, a) At the crown, and b) at the tunnel wall

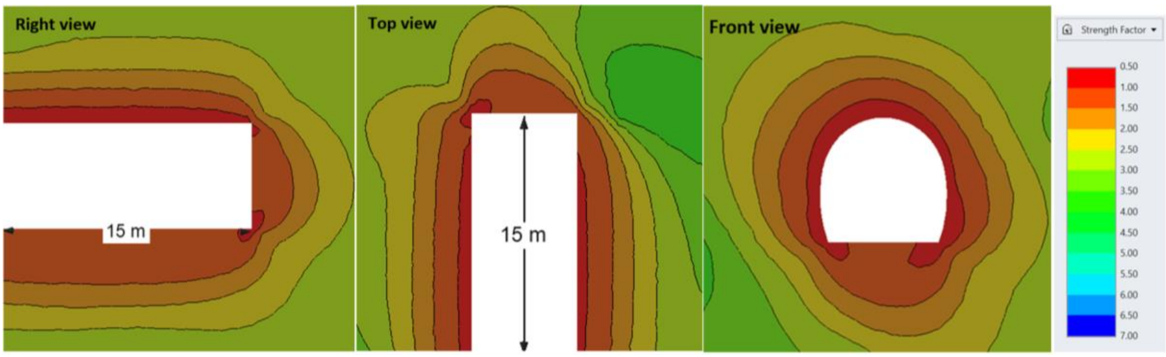

Fig.12 Strength factor contours showing the location and depth of brittle failures surrounding the tunnel. The front view shows the contours 15 m behind the tunnel face

Moreover, the high magnitude of modelled σ_{dev} suggested violent stress-induced failures, but due to the adoption of the drill and blast method, such violent failures were avoided. However, instead of violent stress-induced failures, overbreak occurred, which is due to the transient release of stored strain energy simultaneously with the blast [26]. Still, violent stress-induced failures occurred near the excavation face in Lowari Tunnel. In Fig.13, the SF contours in the selected tunnel section are compared with the excavated cross-sections. The excavated cross-sections show a little bit more over-excavation, but generally, the simulated depth of failures is consistent with the actual. A possible reason for this slight difference could be the amount of overbreak due to the transient release of high stress simultaneously with the blasting.

The release of in-situ stress during blasting is a dynamic process that needs dynamic analysis. The numerical approach used in this study only considers the excavation damaged zone in the presence of a given amount of in-situ stress. It does not include the extent of damage associated with the transient release of the stress. Due to this reason, the simulated depth of failure is a bit smaller than the actual. According to Yang et al. [26], when the in-situ stresses reach 20-50 MPa, the strain rate of the rock mass surrounding the excavation reaches 10^{-1} to 10/s due to the release of in-situ stresses. In terms of estimating the magnitude and orientation of in-situ, it can be inferred that our numerical modelling approach produces acceptable results because the estimated principal stress magnitudes are within the proposed range of in-situ stress for attaining the high strain rate. A stress-induced brittle failure that occurred in the selected tunnel section is also shown in Fig.13. The location and depth of this failure match the simulated stress-induced failure zone.

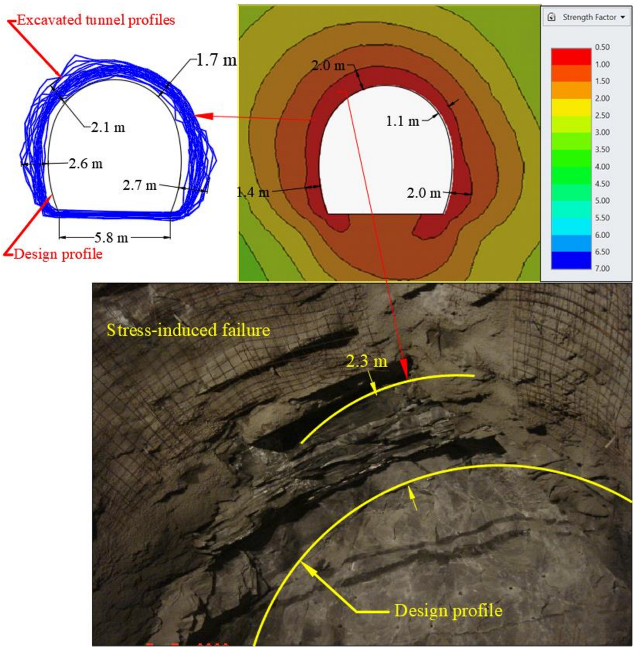

Fig.13 Comparison of stress-induced failure

5. CONCLUSIONS

This study presents a 3D FEM numerical modelling approach that considers the in-situ stress perturbations due to uneven topography. The stress-induced failures in the study tunnel are analysed using numerical and empirical methods, and the results are validated through field observations in a tunnelling case study. Following are the main findings:

- The current topography dominates the in-situ stress in the study area. Thus the assumption that the project site is free from the influence of tectonic forces is applicable here.
- A portion of the overbreak in drill and blast tunnels is attributed to the transient release of the stresses at the excavation face. The slight difference between the simulated and the actual overbreak depth reported in this study is attributed to overbreak that occurred due to the transient release of stresses and is not captured by the numerical approach being used. Thus it is a limitation of numerical modelling.
- The magnitude and orientation of the principal stresses and the corresponding stress induced-failures derived from the numerical approach used in this study generally agree with the empirical approaches established for estimating the stress-induced brittle failures around the underground excavations. Thus, it is inferred that the numerical approach used in this study can produce meaningful results.

This study concentrates on the in-situ stress field, which is mainly under the influence of gravity loading. The application of this modelling approach in geologically complex and tectonically active areas needs further study.

6. ACKNOWLEDGEMENT

The authors would like to acknowledge the findings from the Open Project (LNTCCMA-20210107) from the Key Laboratory of New Technology for Construction of Cities in Mountain Area, Ministry of Education, and the Ministry of Higher Education Malaysia (MOHE) under the Fundamental Research Grant Scheme (FRGS/1/2020/TK0/UTM/03/5) Behavior of Surface Settlement Induced by Tunneling Under Non-Greenfield Condition). The leading author acknowledges the financial support from Higher Education Commission Pakistan under the UESTP scholarship for PhD studies.

7. REFERENCES

[1] Kaiser P. and Kim B.-H. 2015 Characterization of the strength of intact brittle rock considering confinement-dependent failure processes Rock mechanics and rock engineering 48 107-19

[2] Goodman R.E. 1989 Introduction to rock mechanics vol 2: Wiley New York)

[3] Vitali O.P., Celestino T.B. and Bobet A. 2020 Analytical Solution for a Deep Circular Tunnel in Anisotropic Ground and Anisotropic Geostatic Stresses Manuscript under review for publication in a peer-reviewed journal

[4] Martin C. 1997 Seventeenth Canadian geotechnical colloquium: the effect of cohesion loss and stress path on brittle rock strength Canadian Geotechnical Journal 34 698-725

[5] Kaiser P., McCreath D. and Tennant D. 1996 Canadian Rockburst Support Handbook, Mining Re-search Directorate, Sudbury, Canada, 314 p.; also Drift support in burst-prone ground CIM Bulletin 89 131-8

[6] Askaripour M., Saeidi A., Rouleau A. and Mercier-Langevin P. 2022 Rockburst in underground excavations: A review of mechanism, classification, and prediction methods Underground Space

[7] Cai M., Kaiser P., Tasaka Y., Maejima T., Morioka H. and Minami M. 2004 Generalized crack initiation and crack damage stress thresholds of brittle rock masses near underground excavations International Journal of Rock Mechanics and Mining Sciences 41 833-47

[8] Ljunggren C., Chang Y., Janson T. and Christiansson R. 2003 An overview of rock stress measurement methods International Journal of Rock Mechanics and Mining Sciences 40 975-89

[9] Hudson J., Cornet F. and Christiansson R. 2003 ISRM Suggested Methods for rock stress estimation—Part 1: Strategy for rock stress estimation International Journal of Rock Mechanics and Mining Sciences 40 991-8

[10] Amadei B. and Stephansson O. 1997 Estimating in situ Stresses: Springer Science & Business Media)

[11] Sadique M., Zaid M. and Alam M. 2022 Rock tunnel performance under blast loading through finite element analysis Geotechnical and Geological Engineering 40 35-56

[12] Zhang Z., Gong R., Zhang H., Lan Q. and Tang X. 2021 Initial ground stress field regression analysis and application in an extra-long tunnel in the western mountainous area of China Bulletin of Engineering Geology and the Environment 80 4603-19

[13] Ziegler M., Loew S. and Amann F. 2016 Near-surface rock stress orientations in alpine topography derived from exfoliation fracture surface markings and 3D numerical modelling International Journal of Rock Mechanics and Mining Sciences 85 129-51

[14] Figueiredo B., Cornet F., Lamas L. and Muralha J. 2014 Determination of the stress field in a mountainous granite rock mass International Journal of Rock Mechanics and Mining Sciences 72 37-48

[15] Zhang C., Feng X.-T. and Zhou H. 2012 Estimation of in situ stress along deep tunnels buried in complex geological conditions International Journal of Rock Mechanics and Mining Sciences 52 139-62

[16] Li X., Hergert T., Henk A. and Zeng Z. 2022 Contemporary background stress field in the eastern Tibetan Plateau: Insights from 3D geomechanical modelling Tectonophysics 822 229177

[17] Alsabhan A.H., Sadique M.R., Ahmad S., Alam S. and Binyahya A.S. 2021 The effect of opening shapes on the stability of underground tunnels: a finite element analysis GEOMATE Journal 21 19-27

[18] Rehman H., Naji A.M., Ali W., Junaid M., Abdullah R.A. and Yoo H.-k. 2020 Numerical evaluation of new Austrian tunnelling method excavation sequences: A case study International Journal of Mining Science and Technology 30 381-6

[19] Palmstrom A. 2005 Measurements of and correlations between block size and rock quality designation (RQD) Tunnelling and Underground Space Technology 20 362-77

[20] Hoek E., Carter T. and Diederichs M. 2013 Quantification of the geological strength index chart. In: 47th US rock mechanics/geomechanics symposium: American Rock Mechanics Association)

[21] Bieniawski Z.T. 1989 Engineering rock mass classifications: a complete manual for engineers and geologists in mining, civil, and petroleum engineering: John Wiley & Sons)

[22] Rocscience 2022 RSData,. (Toronto), (Canada)

[23] Martin C., Kaiser P. and McCreath D. 1999 Hoek-Brown parameters for predicting the depth of brittle failure around tunnels Canadian Geotechnical Journal 36 136-51

[24] Carter B. 1992 Size and stress gradient effects on fracture around cavities Rock Mechanics and Rock Engineering 25 167-86

[25] Germanovich L. and Dyskin A. 2000 Fracture mechanisms and instability of openings in compression International Journal of Rock Mechanics and Mining Sciences 37 263-84

[26] Lu W., Yang J., Yan P., Chen M., Zhou C., Luo Y. and Jin L. 2012 Dynamic response of rock mass induced by the transient release of in-situ stress International Journal of Rock Mechanics and Mining Sciences 53 129-41